

Article

Mechanical Properties and Fracture Toughness Prediction of Ductile Cast Iron under Thermomechanical Treatment

Mohammed Y. Abdellah ^{1,2,*} , Hamzah Alharthi ¹ , Rami Alfattani ¹ , Dhia K. Suker ¹, H. M. Abu El-Ainin ³, Ahmed F. Mohamed ^{1,4} , Mohamed K. Hassan ^{1,3}  and Ahmed H. Backar ^{1,5} 

¹ Mechanical Engineering Department, College of Engineering and Architecture, Umm Al-Qura University, Makkah 21955, Saudi Arabia; haharhi@uqu.edu.sa (H.A.); rafattni@uqu.edu.sa (R.A.); dksuker@uqu.edu.sa (D.K.S.); afmohamed@uqu.edu.sa (A.F.M.); mkibrahiem@uqu.edu.sa (M.K.H.); ahbackar@uqu.edu.sa (A.H.B.)

² Mechanical Engineering Department, Faculty of Engineering, South Valley University, Qena 83521, Egypt

³ Production Engineering & Design Department, Faculty of Engineering, Minia University, Minia 61111, Egypt; hamed.abuelenin@mu.edu.eg

⁴ Mechanical Engineering Department, Faculty of Engineering, Sohag University, Sohag 82524, Egypt

⁵ Production Engineering Department, Faculty of Engineering, Alexandria University, Alexandria 21544, Egypt

* Correspondence: mohamed_abdalla@eng.svu.edu.eg

Abstract: Temperature has a great influence on the mechanical properties of ductile cast iron or nodular cast iron. A thermomechanical treatment was carried out at various elevated temperatures of 450 °C, 750 °C and 850 °C using a universal testing machine with a tub furnace. Specimens were held at these temperatures for 20 min to ensure a homogeneous temperature distribution along the entire length of the specimen, before a tensile load was applied. Specimens were deformed to various levels of uniform strain (0%, 25%, 50%, 75%, and 100%). These degrees of deformation were measured with a dial gauge attached to a movable cross plate. Three strain rates were used for each specimen and temperature: $1.8 \times 10^{-4} \text{ s}^{-1}$, $9 \times 10^{-4} \text{ s}^{-1}$ and $4.5 \times 10^{-3} \text{ s}^{-1}$. A simple analytical model was extracted based on the CT tensile test geometry and yield stress and a 0.2% offset strain to measure the fracture toughness (J_{IC}). To validate the analytical model, an extended finite element method (XFEM) was implemented for specimens tested at different temperatures, with a strain rate of $1.8 \times 10^{-4} \text{ s}^{-1}$. The model was then extended to include the tested specimens at other strain rates. The results show that increasing strain rates and temperature, especially at 850 °C, increased the ductility of the cast iron and thus its formability. The largest percentage strains were 1 and 1.5 at a temperature of 750 °C and a strain rate of $1.8 \times 10^{-4} \text{ s}^{-1}$ and $9 \times 10^{-4} \text{ s}^{-1}$, respectively, and reached their maximum value of 1.7 and 2.2% at 850 °C and a strain rate of $9 \times 10^{-4} \text{ s}^{-1}$ and $4.5 \times 10^{-3} \text{ s}^{-1}$, respectively. In addition, the simple and fast analytical model is useful in selecting materials for determining the fracture toughness (J_{IC}) at various elevated temperatures and different strain rates.



Citation: Abdellah, M.Y.; Alharthi, H.; Alfattani, R.; Suker, D.K.; Abu El-Ainin, H.M.; Mohamed, A.F.; Hassan, M.K.; Backar, A.H. Mechanical Properties and Fracture Toughness Prediction of Ductile Cast Iron under Thermomechanical Treatment. *Metals* **2024**, *14*, 352. <https://doi.org/10.3390/met14030352>

Academic Editor: Igor Yu. Litovchenko

Received: 25 February 2024

Revised: 10 March 2024

Accepted: 15 March 2024

Published: 19 March 2024



Copyright: © 2024 by the authors. Licensee MDPI, Basel, Switzerland. This article is an open access article distributed under the terms and conditions of the Creative Commons Attribution (CC BY) license (<https://creativecommons.org/licenses/by/4.0/>).

Keywords: ductile cast iron; XFEM; J-integral; fracture toughness; elongation

1. Introduction

Ductile cast iron differs from grey cast iron in that it has spherical graphite inclusions, which give it a certain ductility and a much higher resistance to impact and fatigue. Ductile cast iron with spherical graphite has good performance and durability at high temperatures, it has good mechanical properties, it is easy to cast and it is inexpensive. These properties have made its field of application widespread [1]. There are many competitive applications for ductile cast iron compared to steel [2]. Cast iron is structurally significantly different from steel. This difference is related to the formation and content of carbon or graphite particles. Furthermore, the properties of cast iron depend on and react to the shape of these graphite particles. Ductile cast iron is characterized by a spheroidal graphite shape, which influences both the deformation behavior and the solidification process [3]. Another

advantage of this cast iron is that its structure can be created without any heat treatment by simply controlling the alloying elements. Fatigue fractures, the manufacturing cost and mechanical strength are the most important factors compared to steel [4–8]. Amiri Kasvayee [9] studied the deformation behavior of ductile cast iron in a tensile test using digital image correlation and measured the tensile strength in situ. He described the failure sequence in ductile cast iron as follows: crack formation inside the graphite particles (nodules), followed by decohesion between graphite and the cast iron matrix, formation and growth of voids around the graphite nodule, and finally the connection of micro-cracks that develop into macro-cracks. The graphite nodules act like stress concentration zones in the cast iron matrix, which reduces the overall strength of the ductile cast iron. In another study by Dong et al. [10], other sequences of deformation of ductile cast iron were reported for in situ tensile strength. Ductile cast iron was used in lorry engine exhaust manifolds where creep and creep fatigue properties were severe [11]. The creep damage was caused by voids around the graphite nodule in the matrix of ductile cast iron [12,13], which act as a stress concentration zone, as reported in [9]. On the other hand, Torre et al. [14] studied the mechanical properties as a function of section size, holding temperature and holding time. These factors were the most important parameters of the thermomechanical treatment, and they concluded that the mechanical properties showed different trends depending on the holding temperature and holding time. In addition, the influence of silicon content on mechanical properties was studied by Angella et al. [15]. The degradation of lumpy graphite [16] was more evident with a high silicon content, which reduced the tensile strength. It was concluded that the silicon content promoted oxidation resistance at high temperatures and microstructure durability [17]. Recently, Bendikiene et al. [18] studied the effects of the bainitisation temperature on the toughness, hardness and fatigue resistance of ductile cast iron. They concluded that the hardness decreases with increasing temperature, while the fracture mechanics vary from cleavage ductile to transgranular to ductile dimples at high temperatures.

Kobayashi and Yamada [19] used three-point bend specimens to measure the fracture toughness of ductile cast iron. They used an approximation between 15% scint and initiation fracture toughness to obtain the average fracture toughness J_{IC} (mid) equal to 51.4 kJ/m^2 and they concluded that this was the more reasonable method and also concluded that the dynamic fracture toughness was lower than the static fracture toughness. In a recent study by Artola et al. [20], a special mold pattern was used to obtain a desired standard wedge design and measure the tensile, impact and fracture toughness. Fracture toughness was determined using a three-point bending test based on the previous shape pattern. Variation in the mechanical performance and fracture toughness by maintenance temperature for ductile cast iron was found. On the other hand, alloying elements [21] such as copper and copper–nickel can reduce the fracture toughness of ductile cast iron [22]. Susil K. Putatunda [23,24] investigated the effect of four temperature steps and a two-step bainitisation process on fracture toughness. It was found that the fracture toughness depends only on the ferrite and graphite content of the ductile cast iron and leads to a significant improvement in mechanical properties and fracture toughness. Many papers [25–28] have investigated the effects of heat treatment on the mechanical properties of ductile cast iron. As mentioned earlier, there are many studies investigating the effects of temperature and heat treatment on the mechanical properties and fracture toughness of ductile cast iron, but understanding the effects of the thermomechanical treatment technique on the mechanical properties and fracture toughness needs further investigation.

The fracture toughness of nodular cast iron using a local approach: Researchers employed a finite element method (FEM) and a cohesive zone model to simulate crack propagation and predict fracture toughness. The model accurately predicts fracture behavior under various loading conditions and considers microstructure effects [29]. In one of the two cast irons studied, graphite nodules acted as voids, and the damage evolution related to void growth. In the second cast iron, void nucleation was also considered. The modified Gurson's potential modeled the mechanical behavior, and the tearing test

results could be predicted [30]. In another study [31], they investigated the behavior of cast iron GGG400SiMo under specific conditions involving quasi-static loading at room temperature and high-strain-rate dynamic loading at high temperatures (up to 600 °C). The material's damage behavior was analyzed, and the project aimed to understand its response to varying loading conditions. Additionally, the paper discussed the mechanical properties of cast irons at elevated temperatures, emphasizing the importance of considering creep as a deformation mechanism for high-temperature applications. Creep became a concern above approximately 425 °C [32]. Basurto-Hurtado et al. [33] proposed a novel methodology for generating geometric models that represent the microstructure of ductile cast iron (DCI). The approach involves using image processing algorithms to extract the contours of graphite nodules and employing Bezier curves to smooth the geometric models. Circularity analysis was performed to assess the induced error during discretization, and the impact of design parameters on stress behavior within the DCI microstructure was also investigated using finite element analysis. Notably, increasing the Bezier curve degree decreased circularity and led to higher maximum stresses in the DCI.

Therefore, the present study has three main objectives: The first objective is to measure the tensile strength, elastic modulus and percentage elongation of ductile cast iron at four different temperatures, the second objective is to study the effect of strain rate on ductility and percentage elongation and the last objective is to develop a simple analytical model to calculate the fracture toughness J_{IC} at high deformation temperatures to provide suggestions for material selection.

The work is structured as follows: In the first section, the specifications for ductile cast iron were outlined, then the thermomechanical treatment technique was explained; in the second section, the extended finite element method and the nonlinear J-integral finite element method were derived; in the third part, the results and the relationship between the obtained data were correlated; and in the last section the main conclusions were drawn.

2. Material Characterization

Ductile cast iron, the chemical composition of which is given in Table 1 [34], was obtained from the Egyptian Iron and Steel Company in Helwan, Egypt. The mechanical properties of the tested material were determined by tensile tests at a room temperature of 25 °C and a transverse head speed of 1 mm/min. The tensile strength was measured at 806 MPa, the yield strength at 611 MPa and the percentage elongation was 0.59% according to ASTM E8 [35].

Table 1. Chemical composition of the tested cast iron (wt%) adapted from Ref. [34].

Element	C%	Si%	Mn%	P%	S%	Balanced Fe
Contents (mg)	3.0–3.6	2.0–2.5	0.6	0.04 max	0.04	

3. Experimental Work

The cast iron tensile specimens were circular dog bone specimens of 6 mm diameter with end threads (see Figure 1). The parameters for the thermomechanical treatment (T.M.T.) were the exposure temperature and the degree of deformation. Therefore, during the test, the tensile specimen was heated to the required temperature (450 °C, 750 °C and 850 °C) in the tube furnace of the universal testing machine and held at this temperature for 20 min to ensure a homogeneous temperature distribution over the entire length of the specimen before the tensile load was applied. The specimens were deformed to various uniform degrees of strain (0%, 25%, 50%, 75% and 100%). These degrees of deformation were measured using a dial gauge attached to the moving cross plate. The tests were carried out according to ASTM E8 [35]. The test was performed at three different strain rates: $1.8 \times 10^{-4} \text{ s}^{-1}$, $9 \times 10^{-4} \text{ s}^{-1}$ and $4.5 \times 10^{-3} \text{ s}^{-1}$, these strain rates corresponding to crosshead speeds of 1, 5 and 25 mm/min respectively.

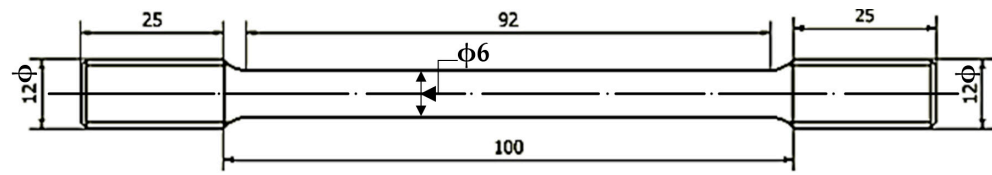


Figure 1. Standard circular dog bone tensile specimen for thermomechanical treatment (dim. mm).

Simple Fracture Toughness Model

The fracture toughness of cast iron is remarkable and important to evaluate, so concepts of elastic–plastic fracture mechanics were applied. The fracture toughness of cast iron is still questionable and needs to be studied. The standards specify many fracture toughness tests such as the Compact Tension Test (CT), Centre Crack and Single Edge Notch Bending [36]. The present model used CT specimens with a thickness of 25 mm according to the ASTM standard [37–39]. This thickness satisfies the following equation:

$$B, a \geq 2.5 \left(\frac{K_Q}{\sigma_{ys}} \right)^2 \quad (1)$$

The model relates the simple tension test data, both yield stress σ_y , the corresponding 0.2% offset strain $\epsilon_{0.2}$ and critical crack opening displacement (δ_{Cr}), at which failure occurs according to the following equation [40]:

$$\delta_{Cr} = t\epsilon_{0.2} \quad (2)$$

The (t) value had been studied in many works [40,41], and Hahn and Rosenfield [42,43] suggested this value was the specimen thickness B . Therefore, it was selected to be equal 25 mm as the CT specimen. After critical crack opening, displacement (δ_{Cr}) is calculated then substituted into the following equation to calculate the surface release energy G_{IC} [44,45]:

$$G_{Ic} = J_{Ic} = \int \sigma_{un} \delta_{cr} \quad (3)$$

At crack initiation for a ductile fracture with a small plastic zone ahead of the crack tip, initiation G_{Ic} can be considered equal J_{Ic} [36].

4. Finite Element Modeling

Finite element modeling was performed to obtain the J-integral energy based on elastic–plastic fracture mechanics. Two independent finite element methods were considered to obtain satisfactory results for the fracture toughness of ductile cast iron at a room temperature of 25 °C. One of them is the nonlinear J-integral method based on a near crack, which is a fictitious closed crack that can open during the analysis; the second method is the linear extended finite element method based on an enhancement function and considering mesh-free rules. For both models, the area CT, shown in Figure 2, was used [46]. The sample CT had the dimensions shown in Figure 2a and a thickness of 25 mm. The domain FE consisted of 40,375 elements with a node size of 0.57 for region A, while the rest of the sample had a size of 5 mm to reduce computation time. The convergence of the model was previously investigated [47] and they found that the mesh size had less influence for small sample dimensions. A linear brick with eight nodes, reduced integration and hourglass control (C3D8R), with a hex shape and of a linear 3D stress element type (see Figure 2b), was studied. The material properties of the ductile cast iron used are listed in Table 2 and were determined by a simple tensile test. The linear XFEM used the maximum principal stress (Maxps) theory for failure, which was the yield stress σ_y , MPa, while the damage assessment was the maximum displacement at failure. This was chosen so that the displacement was the same at 0.2% offset strain. The XFEM was used for all other thermomechanical temperatures due to its simplicity and did not require mesh refinement.

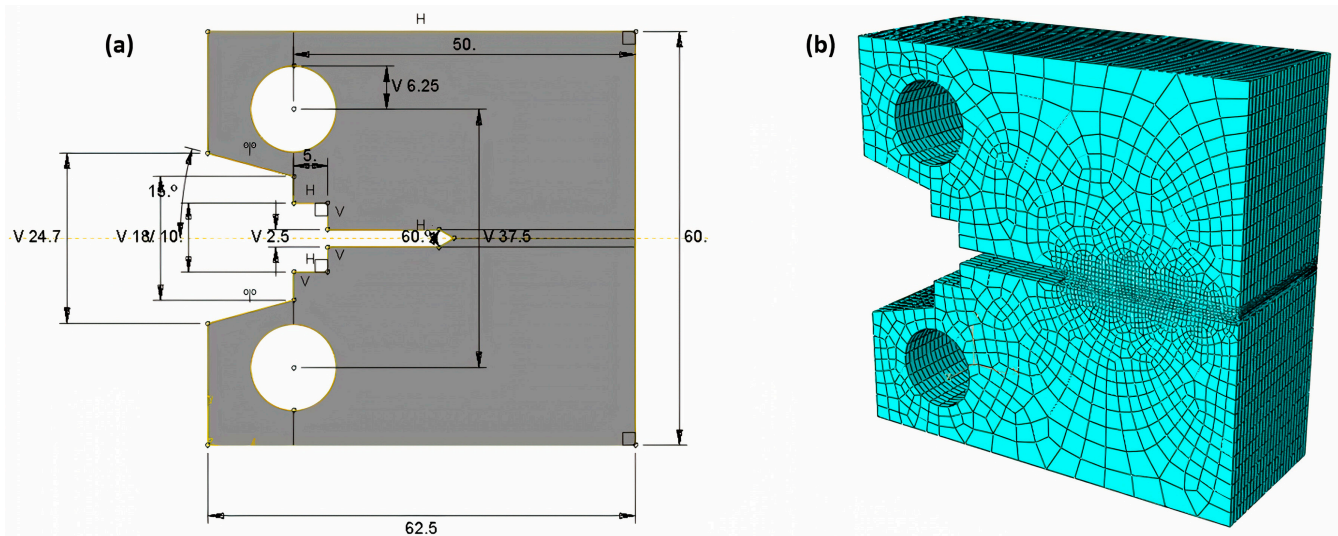


Figure 2. Finite element domain (a) with dimension (in mm); (b) mesh domain.

Table 2. Average mechanical properties of ductile cast iron at different temperature for $1.8 \times 10^{-4} \text{ s}^{-1}$ strain rate.

Properties	Temp.	25 °C	450 °C	750 °C	850 °C
Young modulus E, GPa		169.3	183.7	95.5	90.67
Ultimate strength σ_u , MPa		806	710	244.82	87.4
Yield stress σ_y , MPa		611	450	156	21.27
Fracture strain % ϵ_f		0.59	0.65	1	0.95
Yield strain 0.2% ϵ		0.36	0.25	0.15	0.05
Stiffness stress K		1412	1445	575	575
Strain hardening coefficient n		0.08	0.123	0.13	0.36

5. Results and Discussion

5.1. Effect of Temperature

Figures 3a, 4a and 5a show the relationship between stress and strain for the tensile test on ductile cast iron at a strain rate of $1.8 \times 10^{-4} \text{ s}^{-1}$, $9 \times 10^{-4} \text{ s}^{-1}$ and $4.5 \times 10^{-3} \text{ s}^{-1}$, respectively. It can be clearly seen that as the temperature increases, the strength and modulus of elasticity decrease while the ductility increases, which is represented by the percentage of elongation at the break or the percentage strain. Temperature plays a significant role in altering material behavior. While the strength and modulus decrease, ductility improves, as reflected in the elongation at break or the percentage strain. Assuming that increasing the strain rates improve the deformation behavior of cast iron and increase ductility, the average percentage strain for 850 °C reached 2.2% at a strain rate of $4.5 \times 10^{-3} \text{ s}^{-1}$, as shown in Tables 3 and 4. When cast iron is heated to higher temperatures in the range of 673–773 K, the phenomenon of embrittlement occurs [48,49]. The embrittlement is caused by the segregation of elements P, S, etc., at the grain boundary of the cast iron. The strain hardening coefficient and material stiffness was measured on the log–log scale of Figures 3b, 4b and 5b for the $1.8 \times 10^{-4} \text{ s}^{-1}$, $9 \times 10^{-4} \text{ s}^{-1}$ and $4.5 \times 10^{-3} \text{ s}^{-1}$ strain rate, respectively.

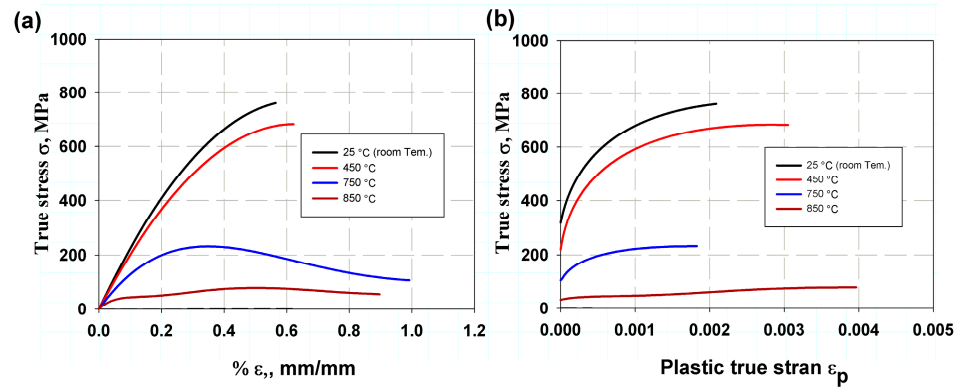


Figure 3. Relation variation with different temperatures at $1.8 \times 10^{-4} \text{ s}^{-1}$ strain rate: (a) stress and strain; (b) plastic stress and plastic strain.

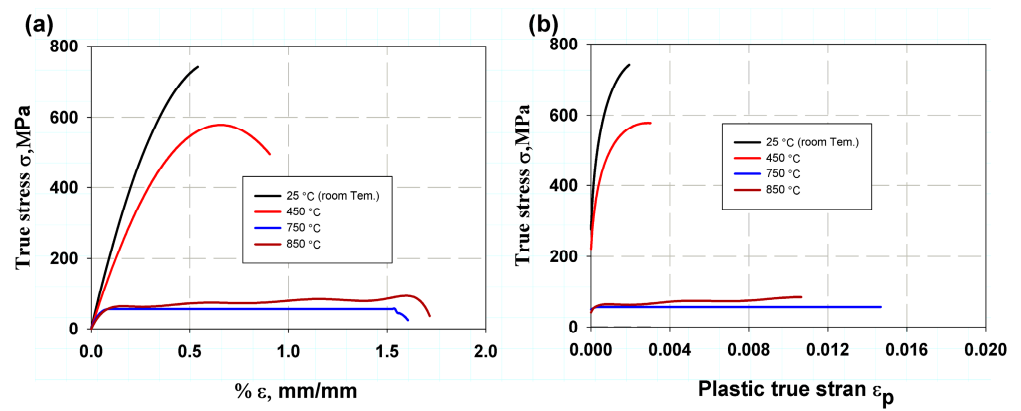


Figure 4. Relation variation with different temperatures at $9 \times 10^{-4} \text{ s}^{-1}$ strain rate: (a) stress verse strain; (b) plastic stress verse plastic strain.

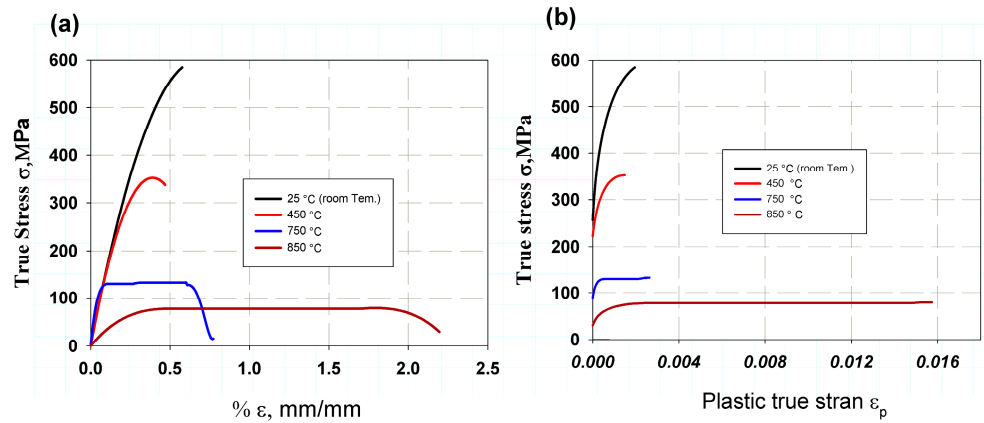


Figure 5. Relation variation with different temperatures at $4.5 \times 10^{-3} \text{ s}^{-1}$ strain rate: (a) stress verse strain; (b) plastic stress verse plastic strain.

Table 3. Average mechanical properties of ductile cast iron variation at different temperatures for $9 \times 10^{-4} \text{ s}^{-1}$ strain rate.

Properties	Temp.	25 °C	450 °C	750 °C	850 °C
Young modulus E, GPa		34.6	29.35	24.43	17.42
Ultimate strength σ_u , MPa		737.6	565	130	92
Yield stress σ_y , MPa		474.1	442	46	61.36
Fracture strain % ϵ_f		0.55	0.91	1.5	1.7
Yield strain 0.2% ϵ		0.25	0.32	0.035	0.073
Stiffness stress K		1479	912	154	107
Strain hardening coefficient n		0.11	0.08	0.11	0.1

Table 4. Average mechanical properties of ductile cast iron variation at different temperatures for $4.5 \times 10^{-3} \text{ s}^{-1}$ strain rate.

Properties	Temp.	25 °C	450 °C	750 °C	850 °C
Young modulus E, GPa		29.34	15.97	13.18	0.903
Ultimate strength σ_u , MPa		523	377	63.06	73.14
Yield stress σ_y , MPa		283	207	113	63
Fracture strain ϵ_f		0.59	0.49	0.69	2.2
Yield strain 0.2% ϵ		0.21	0.16	0.054	0.16
Stiffness stress K		2951	1258	199	114
Strain hardening coefficient n		0.23	0.18	0.069	0.079

It can be observed that the strain hardening coefficient increases with increasing temperature. For deformations with lower strain rates, the strain hardening coefficient is a measure of the hardening of the material with strain. Therefore, with increasing temperature, good ductility is achieved when the strain is better distributed over regions where local accumulation of strain is reduced [50]. At higher strain rates, the strain hardening coefficient shows different tendencies, as the rapid strain rate leads to a sudden or dynamic elongation of the grain and the bonds between the atoms, which reduces both the strength and the strain hardening coefficient. Rapid strain rates cause the dynamic elongation of grains and weaken atomic bonds, resulting in a decreased strength and strain hardening coefficient. Understanding these effects is crucial for designing materials that perform well under varying loading conditions [51]. The true stress and true strain curves, shown in the previous figures, were corrected using a second-order polynomial [50], as the scatter in the measurement may increase and affect the obtaining of good mechanical data. The stiffness stress and yield stress decreased with increasing temperature for all strain rates tested. The larger average percentage strain was 1 and 1.5 at a deformation temperature of 750 °C for a strain rate of $1.8 \times 10^{-4} \text{ s}^{-1}$ and $9 \times 10^{-4} \text{ s}^{-1}$, and 1.7 and 2.2 at a deformation temperature of 850 °C for a strain rate of $9 \times 10^{-4} \text{ s}^{-1}$ and $4.5 \times 10^{-3} \text{ s}^{-1}$, respectively (see Tables 2 and 4). As mentioned earlier, it can be seen that the strain rate has a great influence on the flow behavior of ductile cast iron. The relationship between the strain rate and the deformation temperature was analyzed and is shown in Figure 6 according to the recommendations in [52] as follows:

$$\frac{\sigma}{\sigma_0} = \exp(-BT) \quad (4)$$

where (σ) is the tensile strength at T K absolute temperature, (σ_0) is the tensile strength at 0 °K absolute, chosen as 1733 according to [53], and B is a factor depending on the material properties and strain rate. Factor B is measured using the linear regression of

the data in Figure 6. This curve is useful for measuring any tensile strength in the range ($298\text{ K} < T < 1123\text{ K}$).

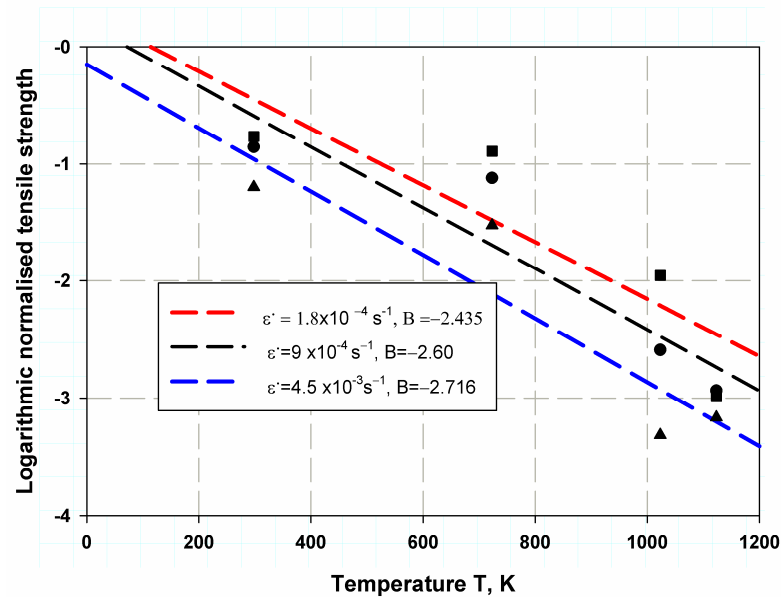


Figure 6. Average nonmilled tensile strength relation with the absolute thermomechanical temperature.

Using a scanning electron microscope (SEM) (manufacturer, city, and country), a micro examination of the fracture surfaces was carried out and is shown in Figure 7. In the brittle fracture shown in Figure 7a, the fracture surface was rough, and the damage could propagate through voids originating from graphite nodules as nuclei. This is due to the fact that the interfacial detachment was weak and therefore the surface had many graphite nodules [49]. After the linear void sequence coalesced, oval shear dimples formed and the fracture surface became smoother and flatter (Figure 7b). The number of dimples and their sizes increased with the test temperature (see Figure 7c,d). The increase in dimple size and number with the rising test temperature in a ductile fracture resulted from enhanced plasticity, energy dissipation, microstructural changes, and specific material behaviors. These dimples serve as visual evidence of the material's response to stress and deformation during fracture [54,55].

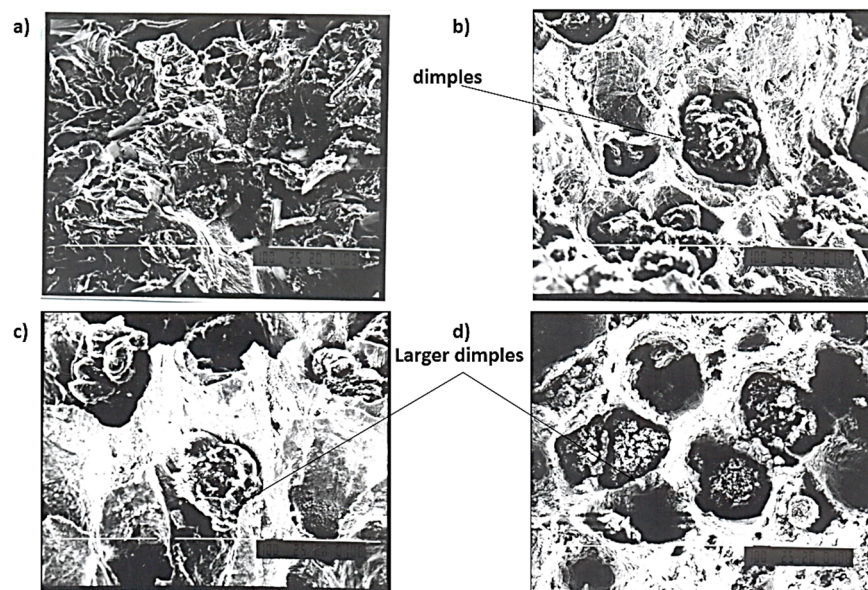


Figure 7. SEM macrograph at room temperature (a) ($25\text{ }^{\circ}\text{C}$), (b) $450\text{ }^{\circ}\text{C}$, (c) $750\text{ }^{\circ}\text{C}$, and (d) $850\text{ }^{\circ}\text{C}$.

5.2. Effect of Strain Rate

Figure 8 shows the relationship between true strain and the strain rate through the tensile test: it is clear it was nearly constant through the whole test data. The strain rate is given by the following equation [56]:

$$\dot{\varepsilon} = \frac{V}{l_f} \quad (5)$$

where V is the cross head speed, and l_f is the instantaneous length, which changed through the whole test. This length is difficult to be experimentally measured; therefore, it can be calculated using the following equation:

$$l_f = l_o \exp(\varepsilon_T) \quad (6)$$

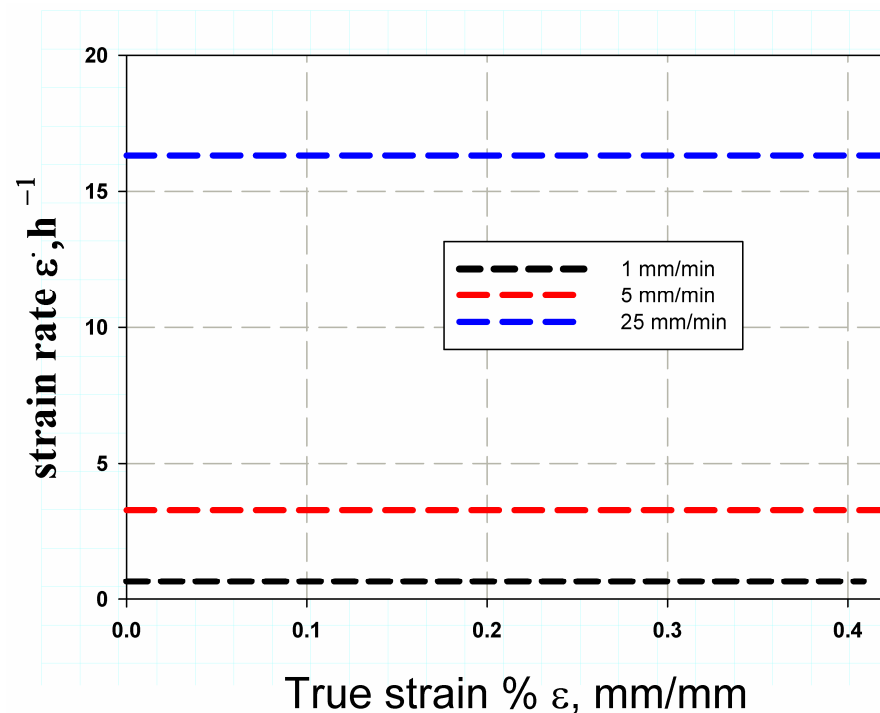


Figure 8. Strain rate variation with true strain through tensile test.

The strain rate for most temperatures took the same trend; this is because the increase in length is related to the same decrease in the cross-sectional area as the volume constant. The relation between the strain rate and tensile strength is the power law relation and related to the following equation [57]:

$$\sigma = \alpha \dot{\varepsilon}^m \quad (7)$$

where α is a constant stress unit (MPa) and m is a material constant; these two constants can be calculated using a linear regression of the log–log scale for the average stress and strain rate curves, as shown in Figure 9. It can be observed that α decreased with increasing temperature (72.5, –174.6 and –248 MPa for 25 °C, 450 °C and 750 °C, respectively). The same trend was maintained for the constant m , which decreased with temperature (–0.13, –0.19 and –0.41 for 25 °C, 450 °C and 750 °C, respectively). Looking at the two curves in Figure 9, it was seen that the sensitivity of the strength-to-strain rate was higher than the sensitivity of the axial strain.

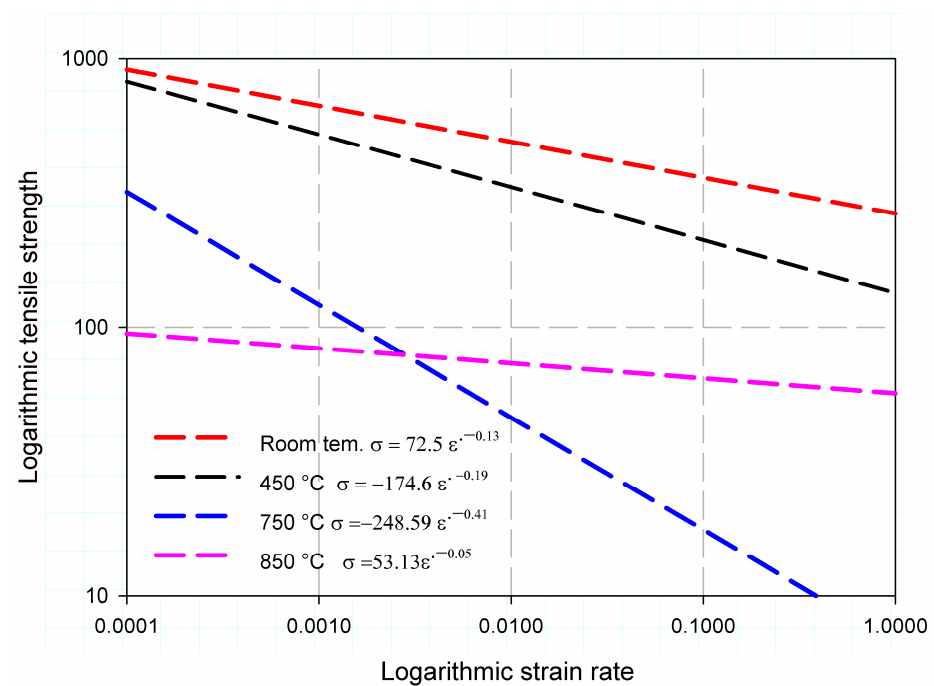


Figure 9. Average strength as a power function of strain rate.

5.3. Fracture Toughness

The fracture toughness, predicted with linear XFEM, was validated with the prediction with the nonlinear J-integral finite element model for ductile cast iron tested at room temperature (25 °C), with a strain rate of $1.8 \times 10^{-4} \text{ s}^{-1}$ (see Figure 10). The value of fracture toughness (surface release energy J_{IC}), determined with XFEM, was 55 kJ/m^2 and the value determined with the J-integral FEM was 54.5 kJ/m^2 . These two values were compared with an experimental value of fracture toughness proposed by Kobayashi and Yamada [19] for ductile cast iron with nearly the same properties, which was measured to be 51.4 kJ/m^2 . Table 5 shows the predicted fracture toughness (J_{IC}) using the presented model based on the fracture strain Equations (2) and (3). The model provided very closed-form values obtained using linear XFEM. The percentage error increased with increasing temperature and reached 27% at a temperature of 850 °C, which was due to the complicated deformation inside a furnace that can lead to misestimation of the fracture strain, e.g., due to slippage of the machine, errors in fixing, etc. It was observed that the values of fracture toughness J_{IC} for ductile cast iron decreased with temperature. This was due to softening and, in addition, ductile fracture leads to the formation of voids in the graphite grains, coalescence and growth. The higher the temperature, the greater the microplastic deformation of the cast iron matrix, the greater the spacing between the graphite grains and the greater the length of the crack tips, which are called graphite nodules, resulting in a decrease in fracture toughness [49]. The model can be extended to other strain rates. Table 5 shows the predicted J_{IC} values for the $9 \times 10^{-4} \text{ s}^{-1}$, and $4.5 \times 10^{-3} \text{ s}^{-1}$ strain rates, respectively. The fracture toughness decreased with increasing strain rate, although the elongation at the break increased. This is due to the fact that as the strain rate increased, a sudden load was applied to the cast iron matrix, so the bond energy dissipated rapidly and the fracture toughness decreased, while fracture toughness decreased with rising strain rate due to reduced plasticity; elongation at break increased because of localized deformation patterns. These contrasting effects highlight the intricate interplay between material behavior and loading conditions [58]. Although the fracture toughness increases with increasing strain rate at 750 °C and 850 °C, this can be attributed to the fact that, at a high temperature, the combination of graphite spheroidization [59], ductile behavior [60], reduced brittleness [59], and increased defect mobility [60] contributes to the improved fracture toughness of cast

iron at higher temperatures. In addition, the flow behaviors of cast iron became more viscoelasticity, therefore behaving with a different trend.

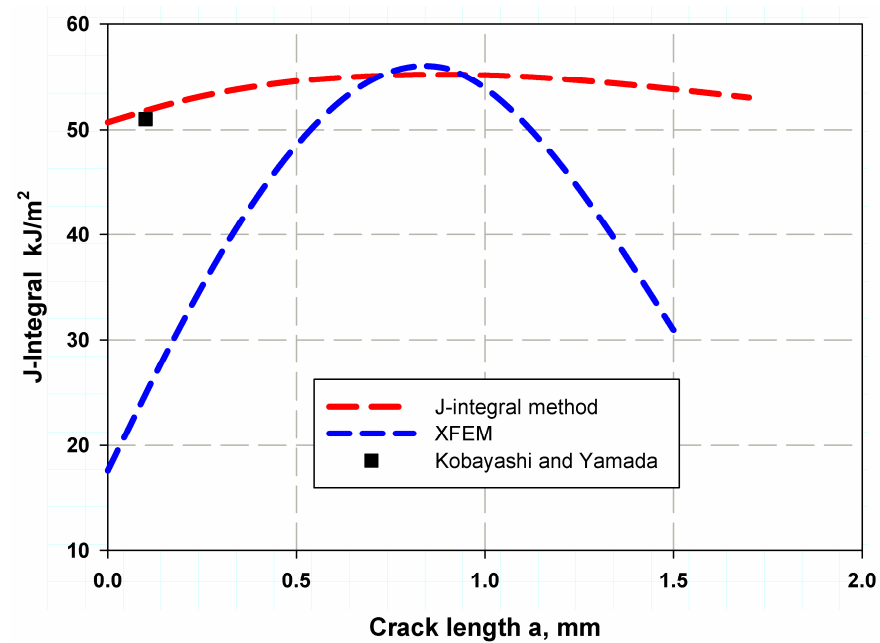


Figure 10. Different finite element model validation with experimental data.

Table 5. Fracture toughness for higher strain rate, based on Equation (2).

Temperature	Strain Rate	$9 \times 10^{-4} \text{ s}^{-1}$	$4.5 \times 10^{-3} \text{ s}^{-1}$
25 °C		29.63	14.85
450 °C		35.36	8.28
750 °C		0.24	1.52
850 °C		1.15	2.52

6. Conclusions

The thermomechanical treatment technique controls the deformation properties of ductile cast iron. It allows the ductile cast iron to stretch up to a maximum of 2.2%. This can open new horizons for the use of cast iron in the hot forming industry to shape crankshafts, gearbox housings, connecting rods, etc. The strain rate was evaluated for its potential to be a reasonable improvement over hot forming ductile cast iron; as a result, ductility was increased and failure modes changed to ductile fracture. By increasing the temperature, good ductility was achieved. The strain was better distributed in areas where the local strain decreased. In addition, as the temperature increased, both the stiffness stress and the yield stress decreased. The effect of temperature on tensile strength was determined using linear regression in the absolute temperature range ($298 \text{ °K} < T < 1123 \text{ °K}$). The linear XFEM and the nonlinear J-integral FEM were good tools for calculating the fracture toughness, with acceptable accuracy. A simple analytical approach to predict the fracture toughness (J_{IC}) was extracted using only the fracture strain in the simple tensile test and the standard test thickness CT of 25 mm. This simple model can be useful for the rapid selection of ductile cast iron to determine its fracture toughness at an elevated temperature from the tensile test data sheet. The data obtained with this simple model were extended to include higher-strain-rate tests.

Author Contributions: Conceptualization, M.Y.A., A.F.M. and R.A.; methodology, M.Y.A. and M.K.H.; software, M.Y.A. and D.K.S.; validation, R.A. and H.M.A.E.-A.; formal analysis, M.Y.A., A.H.B. and

H.A.; investigation, M.Y.A.; resources, R.A.; writing—original draft preparation, M.Y.A.; writing—review and editing, M.Y.A. and H.M.A.E.-A.; supervision, H.A. and A.H.B.; project administration, M.Y.A. and R.A.; funding acquisition, M.K.H. All authors have read and agreed to the published version of the manuscript.

Funding: The authors extend their appreciation to the Deputyship for Research & Innovation, Ministry of Education, in Saudi Arabia for funding this research work through project number IFP22UQU4310022DSR005.

Data Availability Statement: The raw data supporting the conclusions of this article will be made available by the authors on request.

Acknowledgments: The authors would like to thank the undergraduate project team (Eng./Rania Gomma and Eng./Ahmed Ezzat) for helping us in performing the experimental work at the Faculty of engineering, Minia university.

Conflicts of Interest: The authors declare no conflicts of interest.

References

1. Trelles, E.G.; Eckmann, S.; Schweizer, C. Experimental characterization of the short crack growth behavior of a ductile cast iron (DCI GJS-500) affected by intergranular embrittlement at temperatures nearby 400 °C. *Int. J. Fatigue* **2022**, *155*, 106573. [[CrossRef](#)]
2. Fonte, M.; Infante, V.; Freitas, M.; Reis, L. Failure mode analysis of two diesel engine crankshafts. *Procedia Struct. Integr.* **2016**, *1*, 313–318. [[CrossRef](#)]
3. Sertucha, J.; Suárez, R.; Izaga, J.; Hurtado, L.; Legazpi, J. Prediction of solid state structure based on eutectic and eutectoid transformation parameters in spheroidal graphite irons. *Int. J. Cast Met. Res.* **2006**, *19*, 315–322. [[CrossRef](#)]
4. Asi, O. Failure of a diesel engine injector nozzle by cavitation damage. *Eng. Fail. Anal.* **2006**, *13*, 1126–1133. [[CrossRef](#)]
5. Hou, X.-q.; Li, Y.; Jiang, T. Fracture failure analysis of ductile cast iron crankshaft in a vehicle engine. *J. Fail. Anal. Prev.* **2011**, *11*, 10–16. [[CrossRef](#)]
6. Moore, D.; Packer, K.; Jones, A.; Carlson, D. Crankshaft failure and why it may happen again. *Pract. Fail. Anal.* **2001**, *1*, 63–72. [[CrossRef](#)]
7. Mottitschka, T.; Pusch, G.; Biermann, H.; Zybell, L.; Kuna, M. Influence of graphite spherical size on fatigue behaviour and fracture toughness of ductile cast iron EN-GJS-400-18LT. *Int. J. Mater. Res.* **2012**, *103*, 87–96. [[CrossRef](#)]
8. de La Torre, U.; Lacaze, J.; Sertucha, J. Chunky graphite formation in ductile cast irons: Effect of silicon, carbon and rare earths. *Int. J. Mater. Res.* **2016**, *107*, 1041–1050. [[CrossRef](#)]
9. Kasvayee, K.A. Microstructure and Deformation Behaviour of Ductile Iron under Tensile Loading. Ph.D. Thesis, School of Engineering, Jönköping University, Jönköping, Sweden, 2015.
10. Dong, M.; Prioul, C.; François, D. Damage effect on the fracture toughness of nodular cast iron: Part I. Damage characterization and plastic flow stress modeling. *Metall. Mater. Trans. A* **1997**, *28*, 2245–2254. [[CrossRef](#)]
11. Xiang, S.; Jonsson, S.; Babu, R.P.; Zhu, B.; Odqvist, J. Influence of tension and compression dwell on the creep-fatigue properties of the austenitic cast iron Ni-resist D5S. *Mater. Sci. Eng. A* **2021**, *814*, 141179. [[CrossRef](#)]
12. Öberg, C.; Zhu, B.; Jonsson, S. Creep behaviour, creep damage and precipitation in the austenitic ductile cast iron D5S at 750 °C. *Mater. Sci. Eng. A* **2021**, *802*, 140662. [[CrossRef](#)]
13. Öberg, C. Creep Behavior of High Temperature Cast Materials for Exhaust Applications. Ph.D. Thesis, KTH Royal Institute of Technology, Stockholm, Sweden, 2020.
14. de la Torre, U.; González-Martínez, R.; Méndez, S. Effect of the section size, holding temperature and time on the kinetics of the ausferritic transformation and mechanical properties of as-cast ausferritic ductile iron. *Mater. Sci. Eng. A* **2020**, *788*, 139536. [[CrossRef](#)]
15. Angella, G.; Taloni, M.; Donnini, R.; Zanardi, F. The Correlation between Solidification Rates, Microstructure Integrity and Tensile Plastic Behaviour in 4.2 wt.% Silicon Strengthened Ductile Iron. *J. Cast. Mater. Eng.* **2022**, *6*, 1–8. [[CrossRef](#)]
16. Pacha-Gołębiowska, H.; Piekarska, W. Mechanical properties of ductile cast iron relation to the charge elements. *Proc. IOP Conf. Ser. Mater. Sci. Eng.* **2021**, *1199*, 012022. [[CrossRef](#)]
17. Wu, X.; Quan, G.; MacNeil, R.; Zhang, Z.; Sloss, C. Failure mechanisms and damage model of ductile cast iron under low-cycle fatigue conditions. *Metall. Mater. Trans. A* **2014**, *45*, 5085–5097. [[CrossRef](#)]
18. Bendikiene, R.; Ciuplys, A.; Cesnavicius, R.; Jutas, A.; Bahdanovich, A.; Marmysh, D.; Nasan, A.; Shemet, L.; Sherbakov, S. Influence of Austempering Temperatures on the Microstructure and Mechanical Properties of Austempered Ductile Cast Iron. *Metals* **2021**, *11*, 967. [[CrossRef](#)]
19. Kobayashi, T.; Yamada, S. Evaluation of static and dynamic fracture toughness in ductile cast iron. *Metall. Mater. Trans. A* **1994**, *25*, 2427–2436. [[CrossRef](#)]
20. Artola, G.; Monzón, A.; Lacaze, J.; Sertucha, J. Tensile properties and fracture toughness at service temperatures of an optimized pearlitic ductile iron alloy for automotive crankshafts. *Mater. Sci. Eng. A* **2022**, *831*, 142206. [[CrossRef](#)]

21. Boulifa, I.; Hadji, A. Study of the influence of alloying elements on the mechanical characteristics and wear behavior of a ductile cast iron. *Frat. Ed Integrità Strutt.* **2021**, *15*, 74–83. [[CrossRef](#)]
22. Eric, O.; Sidjanin, L.; Miskovic, Z.; Zec, S.; Jovanovic, M. Microstructure and toughness of CuNiMo austempered ductile iron. *Mater. Lett.* **2004**, *58*, 2707–2711. [[CrossRef](#)]
23. Putatunda, S.K. Influence of austempering temperature on fracture toughness of a low manganese Austempered Ductile Iron (ADI). *Mater. Manuf. Process.* **2001**, *16*, 245–263. [[CrossRef](#)]
24. Putatunda, S.K. Development of austempered ductile cast iron (ADI) with simultaneous high yield strength and fracture toughness by a novel two-step austempering process. *Mater. Sci. Eng. A* **2001**, *315*, 70–80. [[CrossRef](#)]
25. Sckudlarek, W.; Krmasha, M.N.; Al-Rubaie, K.S.; Preti, O.; Milan, J.C.; da Costa, C.E. Effect of austempering temperature on microstructure and mechanical properties of ductile cast iron modified by niobium. *J. Mater. Res. Technol.* **2021**, *12*, 2414–2425. [[CrossRef](#)]
26. Laine, J.; Jalava, K.; Vaara, J.; Soivio, K.; Frondelius, T.; Orkas, J. The mechanical properties of ductile iron at intermediate temperatures: The effect of silicon content and pearlite fraction. *Int. J. Met.* **2021**, *15*, 538–547. [[CrossRef](#)]
27. Wang, Y.; Zhang, Y.; Song, R.; Huang, L.; Pei, Y. Effect of the austenitizing temperature on microstructure evolution and impact toughness of a novel bainite ductile iron. *Met. Mater. Int.* **2021**, *27*, 4014–4022. [[CrossRef](#)]
28. Abdellah, M.Y.; Fadhl, B.M.; Abu El-Ainin, H.; Hassan, M.K.; Backar, A.H.; Mohamed, A.F. Experimental Evaluation of Mechanical and Tribological Properties of Segregated Al-Mg-Si Alloy Filled with Alumina and Silicon Carbide through Different Types of Casting Molds. *Metals* **2023**, *13*, 316. [[CrossRef](#)]
29. Berdin, C.; Haušild, P. Damage Mechanisms and Local Approach to Fracture: Part I: Ductile fracture. In *Transferability of Fracture Mechanical Characteristics*; Springer: Dordrecht, The Netherlands, 2002; pp. 167–180.
30. Berdin, C.; Dong, M.; Prioul, C. Local approach of damage and fracture toughness for nodular cast iron. *Eng. Fract. Mech.* **2001**, *68*, 1107–1117. [[CrossRef](#)]
31. Jing, Z. Prediction of failure of cast iron with dynamic loading and high temperature. *Mater. Sci. Eng. A* **2013**, *566*, 71–81. [[CrossRef](#)]
32. Joshi, A.; Baxevanakis, K.P.; Silberschmidt, V.V. High-temperature creep of cast irons. In *Solid Mechanics, Theory of Elasticity and Creep*; Springer: Berlin/Heidelberg, Germany, 2023; pp. 147–173.
33. Basurto-Hurtado, J.A.; Perez-Soto, G.; Osornio-Rios, R.A.; Dominguez-Gonzalez, A.; Morales-Hernandez, L. A new approach to modeling the ductile cast iron microstructure for a finite element analysis. *Arab. J. Sci. Eng.* **2019**, *44*, 1221–1231. [[CrossRef](#)]
34. Abdellah, M.Y.; Hassan, M.K.; El-Ainin, H.A. Plasticity and formability controlling of cast iron using thermo-mechanical treatment. *Am. J. Mater. Eng. Technol.* **2014**, *2*, 38–42.
35. *ASTM E8*; Standard Test Methods for Tension Testing of Metallic Materials. Annual Book of ASTM Standards. ASTM: West Conshohocken, PA, USA, 2001.
36. Anderson, T.L. *Fracture Mechanics: Fundamentals and Applications*; CRC Press: Boca Raton, FL, USA, 2017.
37. Srinivasan, M.; Seetharamu, S. Fracture toughness of metal castings. In *Science and Technology of Casting Processes*; IntechOpen: London, UK, 2012.
38. Systèmes, D. *Fracture Mechanics Study of a Compact Tension Specimen Using Abaqus/CAE*; Abaqus Technology Brief; Abaqus: Johnston, RI, USA, 2007; pp. 1–7.
39. *ASTM E1737*; Standard Test Method for J-Integral Characterization of Fracture Toughness. Annual Book of ASTM Standards. ASTM: West Conshohocken, PA, USA, 1996.
40. Robinson, J.; Tetelman, A. The relationship between crack tip opening displacement, local strain and specimen geometry. *Int. J. Fract.* **1975**, *11*, 453–468. [[CrossRef](#)]
41. Wells, A. Application of fracture mechanics at and beyond general yielding. *Br. Weld. J.* **1963**, *10*.
42. Hahn, G.T.; Rosenfield, A.R. Local yielding and extension of a crack under plane stress. *Acta Metall.* **1965**, *13*, 293–306. [[CrossRef](#)]
43. Hahn, G.; Rosenfield, A. Sources of fracture toughness: The relation between K_{Ic} and the ordinary tensile properties of metals. In *Applications Related Phenomena in Titanium Alloys*; ASTM International: West Conshohocken, PA, USA, 1968.
44. Abdellah, M.Y.; Alsoufi, M.S.; Hassan, M.K.; Ghulman, H.A.; Mohamed, A.F. Extended finite element numerical analysis of scale effect in notched glass fiber reinforced epoxy composite. *Arch. Mech. Eng.* **2015**, *62*, 217–236. [[CrossRef](#)]
45. Abdellah, M.Y. Comparative Study on Prediction of Fracture Toughness of CFRP Laminates from Size Effect Law of Open Hole Specimen Using Cohesive Zone Model. *Eng. Fract. Mech.* **2018**, *191*, 277–285. [[CrossRef](#)]
46. Abdellah, M.Y.; Sadek, M.G.; Alharthi, H.; Abdel-Jaber, G. Mechanical, thermal, and acoustic properties of natural fibre-reinforced polyester. *Proc. Inst. Mech. Eng. Part E J. Process Mech. Eng.* **2023**, 09544089231157638. [[CrossRef](#)]
47. Mohammed, Y.; Hassan, M.K.; Hashem, A. Finite element computational approach of fracture toughness in composite compact tension specimen. *Int. J. Mech. Mechatron. Eng.* **2012**, *12*, 57–61.
48. Nishi, S.; Kobayashi, T.; Taga, S.; Kurosawa, S. Fragilisation par Revenu de la Fonte a Graphite Spheroidal. Ph.D. Thesis, Université de Lille, Lille, France, 1976.
49. Kobayashi, T. Ductile cast iron. In *Strength and Toughness of Materials*; Springer: Berlin/Heidelberg, Germany, 2004; pp. 89–110.
50. Den Uijl, N.; Carless, L. Advanced metal-forming technologies for automotive applications. In *Advanced Materials in Automotive Engineering*; Elsevier: Amsterdam, The Netherlands, 2012; pp. 28–56.

51. Levy, B.; Van Tyne, C. Effect of a strain-hardening rate at uniform elongation on sheared edge stretching. *J. Mater. Eng. Perform.* **2012**, *21*, 2147–2154. [[CrossRef](#)]
52. Kogoh, S.; Sakai, T.; Asami, K. Temperature dependence of tensile strength and hardness for nodular cast iron and their mutual correlation. *J. Mater. Sci.* **1992**, *27*, 4323–4328. [[CrossRef](#)]
53. Wood, D.; Clark, D. The influence of temperature upon the time delay for yielding in annealed mild steel. *Trans. Am. Soc. Met.* **1951**, *43*, 571–586.
54. Konovalenko, I.; Maruschak, P.; Prentkovskis, O. Automated method for fractographic analysis of shape and size of dimples on fracture surface of high-strength titanium alloys. *Metals* **2018**, *8*, 161. [[CrossRef](#)]
55. Haitao, X.; Dengke, W.; Kaihong, S. Effect of deformation temperature on mechanical properties and microstructure of TWIP steel for expansion tube. *High Temp. Mater. Process.* **2020**, *39*, 63–73. [[CrossRef](#)]
56. Dieter, G.E.; Bacon, D.J. *Mechanical Metallurgy*; McGraw-Hill: New York, NY, USA, 1976; Volume 3.
57. Ma, L.; Daemen, J. Strain rate dependent strength and stress–strain characteristics of a welded tuff. *Bull. Eng. Geol. Environ.* **2006**, *65*, 221–230. [[CrossRef](#)]
58. Yin, B.; Steinke, C.; Kaliske, M. Formulation and implementation of strain rate-dependent fracture toughness in context of the phase-field method. *Int. J. Numer. Methods Eng.* **2020**, *121*, 233–255. [[CrossRef](#)]
59. Pariente, I.; Belzunce, F.; Riba, C.y.J. Mechanical strength and fracture toughness of high chromium white cast irons. *Mater. Sci. Technol.* **2008**, *24*, 981–985. [[CrossRef](#)]
60. Salzbrenner, R.; Van Den Avyle, J.A.; Lutz, T.J.; Bradley, W.L. Fracture Toughness Testing of Ductile Cast Irons. In *Fracture Mechanics: Sixteenth Symposium*; ASTM International: West Conshohocken, PA, USA, 1985.

Disclaimer/Publisher’s Note: The statements, opinions and data contained in all publications are solely those of the individual author(s) and contributor(s) and not of MDPI and/or the editor(s). MDPI and/or the editor(s) disclaim responsibility for any injury to people or property resulting from any ideas, methods, instructions or products referred to in the content.